Structural, spectroscopic, magnetic and electrical characterization of Ca-doped polycrystalline bismuth ferrite, $Bi_{1-x}Ca_xFeO_{3-x/2}$ ($x \leq 0.1$)

Structural, spectroscopic, magnetic and electrical characterization of Ca-doped polycrystalline bismuth ferrite, Bi$_{1-x}$Ca$_x$FeO$_{3-x/2}$ ($x \leq 0.1$)

Kripasindhu Sardar[1]**, Jiawang Hong**[2]**, Gustau Catalan**[3]**, P K Biswas**[4]**,
Martin R Lees**[4]**, Richard I Walton**[1]**, James F Scott**[5] **and
Simon A T Redfern**[5]

[1] Department of Chemistry, University of Warwick, Coventry CV4 7AL, UK
[2] Department of Physics and Astronomy, Rutgers, State University of New Jersey,
136 Frelinghuysen Road, Piscataway, NJ 08854-8019, USA
[3] ICREA and Centre d'Investigacions en Nanociencia'i Nanotecnologia (CIN2), CSIC-ICN,
Campus de la UAB, 08193 Bellaterra (Barcelona), Spain
[4] Department of Physics, University of Warwick, Coventry CV4 7AL, UK
[5] Department of Earth Sciences, University of Cambridge, Downing Street, Cambridge CB2 3EQ, UK

E-mail: satr@cam.ac.uk

Abstract

The crystal structure and physical properties of multiferroic polycrystalline Ca^{2+}-doped BiFeO$_3$ samples have been investigated. The present experimental investigation suggests that Bi$_{1-x}$Ca$_x$FeO$_{3-x/2}$ ($x \leq 0.1$) can be considered as a solid solution between BiFeO$_3$ and CaFeO$_{2.5}$. The oxidation state of Fe in these materials is +3 and charge balance occurs through the creation of oxygen vacancies. For each composition, two structural phase transitions are revealed as anomalies in the variable-temperature *in situ* x-ray diffraction data which is consistent with the well-established high-temperature structural transformation in pure BiFeO$_3$. All compositions studied show antiferromagnetic behaviour along with a ferromagnetic component that increases with Ca^{2+} doping. The resistivities of the Bi$_{1-x}$Ca$_x$FeO$_{3-x/2}$ samples at room temperature are of the order of 10^9 Ω cm and decrease with increasing Ca^{2+} content. Arrhenius plots of the resistivity show two distinct linear regions with activation energies in the range of 0.4–0.7 and 0.03–0.16 eV. A correlation has been established between the critical temperatures associated with the structural phase transitions and the multiferroic properties. A composition of $x = 0.085$ is predicted to show maximum magneto-electric coupling.

(Some figures may appear in colour only in the online journal)

1. Introduction

Over the past few decades BiFeO$_3$ has emerged as the most studied multiferroic material [1–5]. The antiferromagnetic and ferroelectric ordering temperatures of BiFeO$_3$ are ~640 K and 1103 K, respectively. Since both transitions are above room temperature BiFeO$_3$ may have potential applications in devices [3, 4]. Owing to its high spontaneous electrical polarization (~100 μC cm^{-2}) BiFeO$_3$ is also considered as a practical lead-free ferroelectric material [6–8]. On the other hand, the low thermal stability of BiFeO$_3$ provides an obstacle to conventional ceramics processing of this material,

as the processing window is very narrow. The formation of impurity phases such as $Bi_{25}FeO_{39}$ and $Bi_2Fe_4O_9$ provides an additional difficulty in the physical characterization of the paraelectric high-temperature phase [9]. Since part of the problem lies in the volatility of bismuth, doping the A site (Bi site) in $BiFeO_3$ is a key strategy, and there have been plenty of studies on the effect of the replacement of Bi^{3+} with different substituents [10–16]. The doping experiments with Ca^{2+} are of particular interest because they can be exploited to control the band-filling in insulating $BiFeO_3$ thin films, thereby triggering an insulator–metal transition with varying composition [17]. In polycrystalline samples, we have shown recently that the effect of Ca^{2+} doping can be compared to that of hydrostatic pressure on $BiFeO_3$ [18], raising the Néel temperature. The doping-induced convergence between the magnetic Néel temperature and the ferroelectric Curie temperature should lead to increased magneto-electric coupling, and ceramic powder with an A-site composition of $Bi_{0.7}Ca_{0.3}$ shows a converse magneto-electric effect [19].

As regards the crystal structure of Ca^{2+}-doped $BiFeO_3$, Chen *et al* refined materials with up to 20% Ca on the A site as a mixture of a rhombohedral and a disordered cubic phase [20], while Schiemer *et al* have observed the appearance of an ordered perovskite-related phase using transmission electron microscopy [21]. It is also interesting to note that a sample with an A-site composition of $Bi_{0.9}Ca_{0.1}$ has been described by Kothari *et al* as triclinic [22] whereas Khomchenko *et al* have found that for up to 30% Ca doping a rhombohedral structure can adequately describe single-phase material [13, 23, 24].

Here we provide a detailed investigation of the structure–property relationship in $Bi_{1−x}Ca_xFeO_{3−x/2}$ ceramic powders. We show that doping with Ca^{2+} in polycrystalline $BiFeO_3$ affects the high-temperature structural phase transition of polycrystalline $BiFeO_3$ in a manner which is inconsistent with that observed in epitaxial thin films. Doping with Ca^{2+} on the A site of $BiFeO_3$ reduces the number of Bi^{3+} ions which will in turn reduce the collective number of stereo-chemically active $6S^2$ lone pairs. Simultaneously, charge balance occurs through the creation of oxygen vacancies. These affect the degree of off-centring of the FeO_6 octahedra and thus also the multiferroic properties of $BiFeO_3$.

2. Experimental details

2.1. Synthesis

Polycrystalline samples of $Bi_{1−x}Ca_xFeO_{3−x/2}$ were synthesized using a tartaric-acid-based sol–gel process. This technique is particularly useful since it provides better control over the chemical homogeneity of the samples. The synthesis was performed by drying the gel with subsequent calcinations at 873 K followed by sintering at 973 K in the form of a pellet. The processing temperature was kept low in order to prevent thermal decomposition of the $BiFeO_3$. Details of the synthesis process can be found elsewhere [18, 25].

2.2. Characterization

For powder x-ray diffraction (PXRD) analysis, the sintered pellets were ground into fine powder. PXRD data were collected at room temperature using a Bruker D8 Advance x-ray diffractometer operating with Cu Kα_1 ($\lambda = 1.5406$ Å) radiation and a Sol-X energy discriminating detector. *In situ* variable-temperature PXRD patterns were collected using a Bruker D8 Advance set-up for high-temperature measurement, with an MSI furnace and Cu Kα x-ray source in θ–θ geometry. Data were collected with a VÅNTEC 1D position-sensitive detector, which allows rapid data acquisition. Rietveld refinement of the PXRD data was performed using the GSAS-EXPGUI package [26, 27]. Raman spectroscopy data on polished pellets were recorded at room temperature using a Renishaw inVia Raman microscope equipped with an Ar^+ laser with a wavelength of 514.5 nm. Magnetization versus temperature (*M* versus *T*) and applied magnetic field (*M* versus *H*) data were collected over the temperature range 5–400 K in applied magnetic fields of up to 10 000 Oe using a Quantum Design magnetic property measurement system (MPMS) SQUID magnetometer. In an attempt to remove any surface-adsorbed molecular oxygen, the samples were first heated to 400 K in the magnetometer and the sample chamber was then purged and backfilled with helium gas several times. *M* versus *T* data were collected while zero-field-cooled warming (ZFCW) and on field-cooled cooling (FCC). X-ray absorption near-edge structure (XANES) experiments were performed using the B18 beamline of the Diamond Light Source, UK. B18 provides x-ray energies in the range 2.05–35 keV using a fixed-exit, double-crystal monochromator [28]. Typically, $\sim$20 mg of each $Bi_{1−x}Ca_xFeO_{3−x/2}$ sample was mixed with $\sim$80 mg of polyethylene powder and then pressed into 13 mm diameter pellets of $\sim$1 mm thickness. XANES data were collected at the Bi L_{III} and Fe K edges in transmission mode, with ion chambers before and after the sample filled with appropriate mixtures of inert gases to optimize sensitivity. The spectra were measured with a step size equivalent to less than 0.5 eV. Data were normalized using the Athena program [29] with a linear pre-edge and polynomial post-edge background subtracted from the raw $\ln(I_t/I_0)$ data.

The resistivity of the samples was measured from room temperature up to the thermal decomposition temperature of the materials inside a quartz tube furnace. Four platinum wires were attached to the sintered ceramic samples using silver paste, and the resistance was measured using the four-probe method using a Keithley D500 multimeter.

3. Results and discussion

At ambient conditions $BiFeO_3$ is a rhombohedrally distorted perovskite polymorph which can be described in different settings of the rhombohedral space group *R*3*c* (no. 161), although Lebeugle [30] and Schmid [31] have emphasized that, though metrically rhombohedral, the known presence of a magnetic cycloid should strictly lower the symmetry to monoclinic due to magnetostriction. Figure 1 shows

Table 1. Refined pseudo-cubic unit cell lattice parameters of polycrystalline $Bi_{1-x}Ca_xFeO_{3-x/2}$, where $x = 0.0$–0.1 is obtained using different structural models. The goodness of fit of the refinement is also presented. (Note: atomic coordinates for rhombohedral (R) and cubic (C) structures were taken from [32] and [33], respectively.)

	$x = 0.00$	$x = 0.03$	$x = 0.05$		$x = 0.07$		$x = 0.1$	
	R	R	R	C	R	C	R	C
a_p (Å)	3.961 09(23)	3.957 40(10)	3.950 55(12)	3.9489(6)	3.946 56(16)	3.944 22(19)	3.935 27(17)	3.935 95(17)
α (deg)	89.435(7)	89.4811(29)	89.544(4)	90	89.711(7)	90	90.056(33)	90
Vp (Å)^3	62.141(6)	61.9693(26)	61.6499(33)	61.580(17)	61.467(4)	61.360(5)	60.943(5)	60.974(5)
R p	0.091	0.09	0.0847	0.1186	0.0844	0.1157	0.0964	0.0961
χ^2	1.173	1.432	1.461	2.801	1.331	2.364	1.509	1.448

least-squares Rietveld refinement results of the PXRD patterns of $Bi_{1-x}Ca_xFeO_3$. The rhombohedral peak splitting in the PXRD patterns (e.g. between the $(01\bar{1})$ peak at around 31.965° 2θ and the $(10\bar{1})$ peak at approximately 32.130° 2θ) gradually decreases with increasing Ca^{2+} doping. This is consistent with observations of Chen *et al* and Kothari *et al* [20, 22] Bearing in mind the observations of Khomchenko *et al* [13, 14] we have refined the PXRD patterns of the $x = 0.05$–0.1 samples using both rhombohedral and cubic structural models. The atomic coordinates used in this study for rhombohedral and cubic structures have been taken from [32] and [33], respectively. Interestingly, both the cubic and the rhombohedral models give equally good fits (as judged by the goodness-of-fit parameters in table 1) for the calcium-doped samples with $x = 0.05$–0.1. We note that this cannot be taken as evidence for one or other model; rather the purpose of our study is to determine the variation in spontaneous strain below the temperature–composition-driven phase transitions, and we emphasize that, for the purpose of determining cell parameter variations, our models (while not reflecting subtleties such as supercell relationships, for which neutron studies would be preferred) are sufficient. In table 1 we show the refined lattice parameters along with the goodness-of-fit parameters for the different structural models employed in this study. In figures 2(a) and (b) we compare the pseudo-cubic unit cell parameter (a_p) and volume (V_p), of the $Bi_{1-x}Ca_xFeO_{x-3/2}$ samples ($0 \leq x \leq 0.2$) with three different independent studies in the literature [20, 21, 23]. Figure 2(a) and (b) reveal that the lattice parameters and cell volume of the present samples, although determined using laboratory PXRD data, correlate well with those obtained using neutron and synchrotron diffraction techniques. The decrease in the lattice parameter and unit cell volume is almost linear for $x \leq 0.2$, as expected due to the stoichiometric replacement of Bi^{3+} with a smaller ionic radii substituent (in this case Ca^{2+}). A comparison of the lattice parameters themselves reveals a single-phase solid solution for $0 \leq x \leq 0.2$. We note that a high solubility limit of Ca^{2+} in single-phase $Bi_{1-x}Ca_xFeO_{3-x/2}$ samples is expected. Indeed, $Bi_{0.5}Ca_{0.5}FeO_{2.75}$ is known to be stabilized as a perovskite structure under certain synthesis conditions [34]. The effect of Ca^{2+} doping is further reflected in the Raman spectra of the $x = 0.0$–0.1 samples as shown in figure 3. It is clear that increasing x gives rise to broad and less intense Raman bands associated with the normal modes in pure $BiFeO_3$, while there is no appearance of

extra bands in the doped samples. Thus, it appears that doping with Ca^{2+} in $BiFeO_3$ affects the perovskite-related phonon modes which are associated with a tilting of the FeO_6 octahedra, the motion of oxygen atoms associated with the Bi site and the off-centring of the Fe from its special crystallographic position [35]. A similar effect is also observed when $BiFeO_3$ is doped with rare-earth ions like, Nd^{3+}, Sm^{3+} and Gd^{3+} [36]. Thus, a combination of the Raman spectroscopy and the PXRD data suggest that our samples are single-phase members of a solid solution between $BiFeO_3$ and $CaFeO_{2.5}$ [21, 34].

The determination of the oxidation state of Fe is important as this can provide indirect evidence of the oxygen stoichiometry in doped $BiFeO_3$. Figure 4 shows that the Fe K-edge XANES spectra obtained for the Ca^{2+}-doped samples are very similar to the spectra of Fe_2O_3 and quite unlike, for example, that of Fe_3O_4. Here, of course, we do not expect a mixture of Fe^{2+} and Fe^{3+} as seen in magnetite, but the comparison remains useful because it provides an indication of the edge shift anticipated with changes in Fe-oxidation state. A similar shift, but to higher energy, would be expected if Fe^{4+} were present since the edge shift for Fe is rather linear from 2+ to 3+ to 4+. There is no noticeable difference in the position of the absorption edge among our samples with varying doping concentration. The edge position for all the samples is around 7124 eV (determined from the first derivative of the absorption with respect to energy or the inflection point in figure 4(b)) which is characteristic of Fe^{3+} [37, 38] and is related to the 1s to 4s transition. The pre-edge feature (denoted as P in figure 4(b)) that arises from a dipole-forbidden transition (1s to 3d) in Fe is weak although more pronounced in the $x = 0.1$ sample. A considerable post-edge feature (C) is seen which is associated with a 1s to 4p transition. We note that any change in the oxidation state of Fe is expected to give a detectable shift in the absorption edge [39]. Thus, the Fe in these samples is in the 3+ oxidation state. The increase in the number of dipole-forbidden transitions in the $x = 0.1$ sample may be due to an increase in the number of oxygen vacancy-related distortions of FeO_6 octahedra. Interestingly, the lattice distortion due to the steric effect of the A cation (reduction of average ionic radius) is reduced, as reflected in progressive reduction of rhombohedral distortion in the doped samples as discussed above. A similar but more pronounced effect is observed in Ta-doped $BiFeO_3$ [40] and in epitaxial $BiFeO_3$ thin films [41]. Additionally, Bi L_{III} XANES spectra
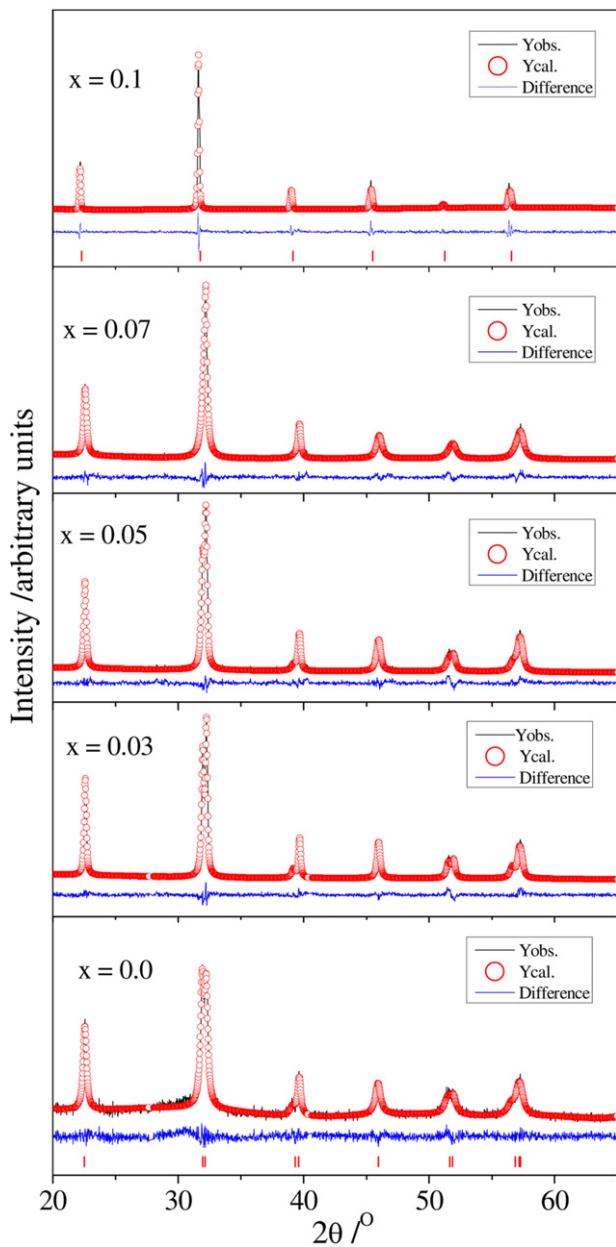
Figure 1. Results from the Rietveld refinement of laboratory PXRD patterns of $Bi_{1-x}Ca_xFeO_{3-x/2}$. Samples with $x = 0.0$–0.07 are refined with space group $R3c$ while cubic space group $Pm\bar{3}m$ is used for $x = 0.1$. Tick marks correspond to the expected reflection positions of respective structures.

Figure 2. Variation of the lattice parameter a_p and unit cell volume V_p with x in $Bi_{1-x}Ca_xFeO_{3-x/2}$ derived from PXRD analysis and compared with literature-reported values obtained from analysis of powder neutron diffraction (PND) and synchrotron x-ray diffraction (SXRD) by Chen *et al* [20], PXRD by Khomchenko *et al* [23] and Schiemer *et al* [21].

Figure 3. Raman spectra recorded on polycrystalline $Bi_{1-x}Ca_xFeO_{3-x/2}$ using a 514.5 nm laser.

analysis of these doped samples show that all Bi atoms are in the 3+ oxidation state, suggesting that Ca^{2+} doping in $BiFeO_3$ creates oxygen vacancies to maintain the charge balance.

Figure 5 shows the DC magnetization versus temperature behaviour for $x = 0.0$–0.1 samples in an applied magnetic field of 10 000 Oe. The nearly temperature-independent magnetization behaviour seen between 300 and 50 K is expected of antiferromagnetic $Bi_{1-x}Ca_xFeO_{3-x/2}$ samples well below their Néel temperatures (T_N). A small rise in the magnetization below 50 K is observed for the $x = 0.0$ and 0.03 samples, and is attributed to an
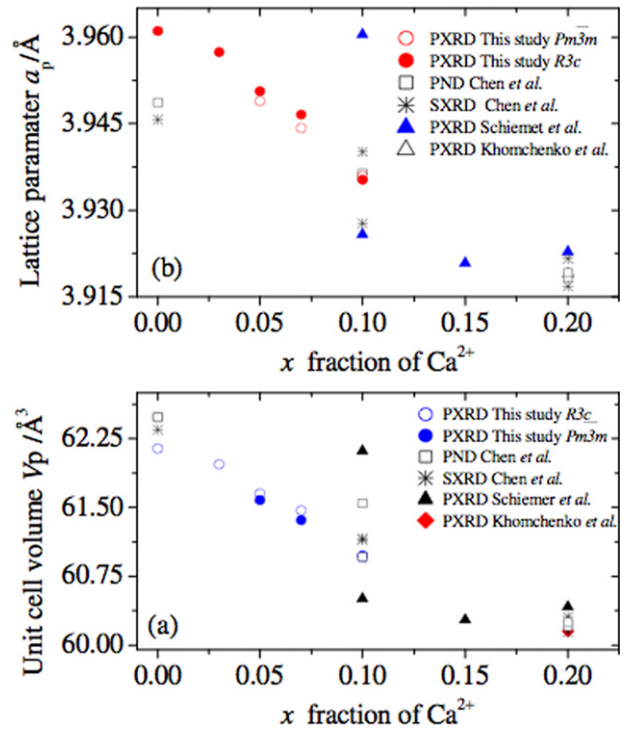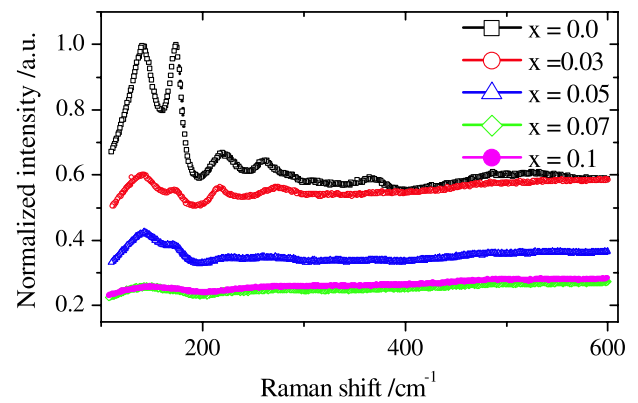
unidentified paramagnetic impurity phase [42]. The formation of paramagnetic impurities is suppressed with calcium doping since samples within $0.05 \leq x \leq 0.1$ shows almost no rise in magnetic moment in the low-temperature region. There is also a subtle magnetic anomaly at $\sim$50 K which has also been seen in previous reports [20]. One possible explanation for this type of anomaly in the temperature region of 50–70 K could be an antiferromagnetic transition of adsorbed molecular oxygen on the surface of small-grain samples. Another possibility worth mentioning is that this type of feature may arise from $CaFeO_{2.5}$ impurities, which exhibit a similar magnetic
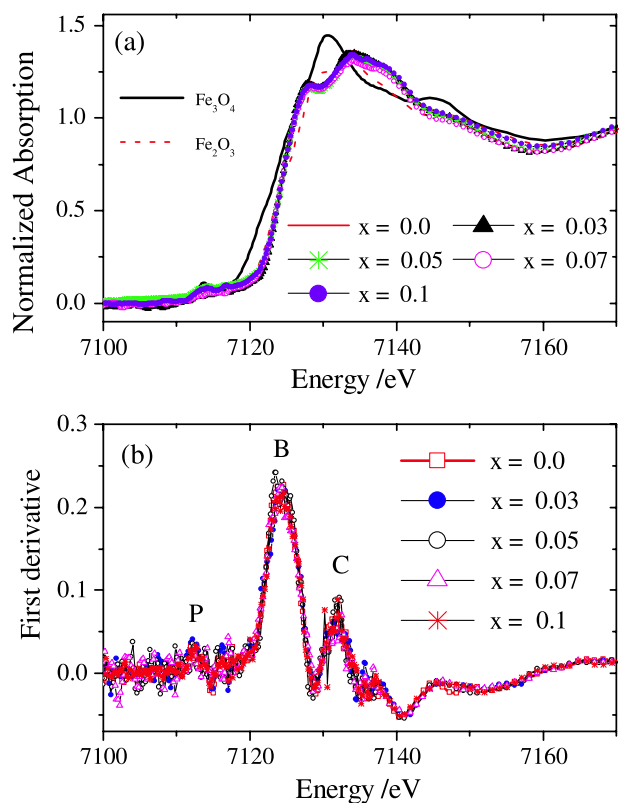
Figure 4. (a) The normalized Fe K-edge XANES spectra and (b) its first derivative with respect to energy for polycrystalline $Bi_{1-x}Ca_xFeO_{3-x/2}$ samples compared with suitable standards. Features in the post-edge, edge and pre-edge regions are marked with C, B and P.

Figure 5. Variation of magnetization with temperature in polycrystalline $Bi_{1-x}Ca_xFeO_{3-x/2}$. In each case DC magnetization data were recorded with an applied magnetic field of 10 kOe.

anomaly due to a change in the easy axis of magnetization between 40 and 60 K [43, 44]. However, it is unlikely that the system is phase-separated into $CaFeO_{2.5}$ and $BiFeO_3$ at such low Ca^{2+} doping levels.

Figure 6 shows M versus H loops collected at 5 K. A significant hysteresis develops with increasing mole fraction of Ca^{2+}. The difference between the ZFCW and FCC curves also increased with x. This can be understood as a suppression of the magnetic spin spiral arrangement of $BiFeO_3$, which leads to a weak (canting) ferromagnetic moment caused by the Dzyaloshinskii–Moriya interaction. The unwinding of the spiral and appearance of a canted moment has previously been reported as a function of pressure, strain or chemical doping [45]. In our case, it is not clear whether the key factor is the reduction of the stereochemical activity of the Bi site or the 'chemical pressure' effect of the substitution for a smaller ion; the chances are that both factors are at play here.

The high-temperature structural phase transition in these Ca^{2+}-doped $BiFeO_3$ samples has been investigated using the variable-temperature *in situ* PXRD technique. Figures 7 and 8 show the variation of the pseudo-cubic lattice parameter and rhombohedral angle (α), respectively, for samples within $x = 0.0 - 0.1$. Clearly the rhombohedral angle is almost $90°$ for $x = 0.07$ and 0.1, indicating that the rhombohedral distortion in these samples is negligible. Additionally, variations in the pseudo-cubic lattice parameter and the rhombohedral angle
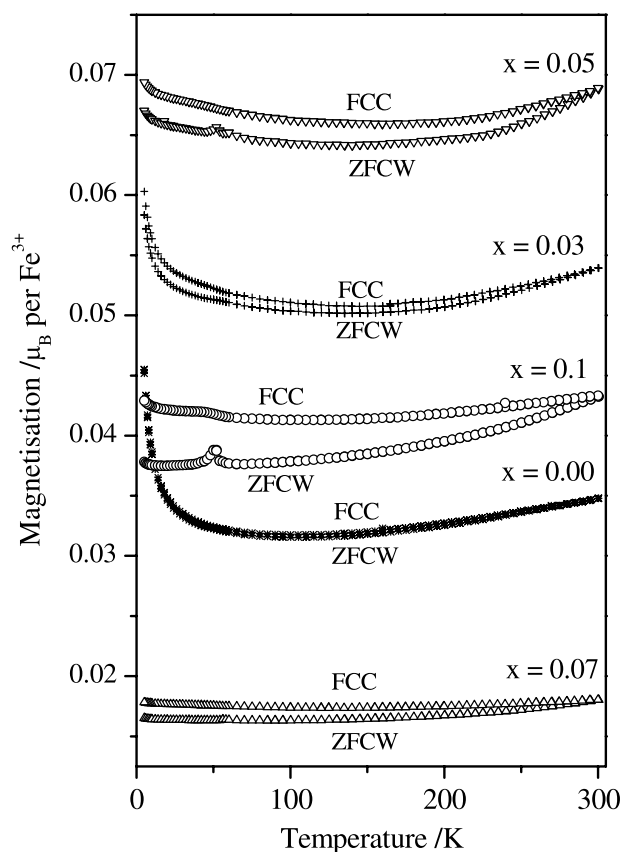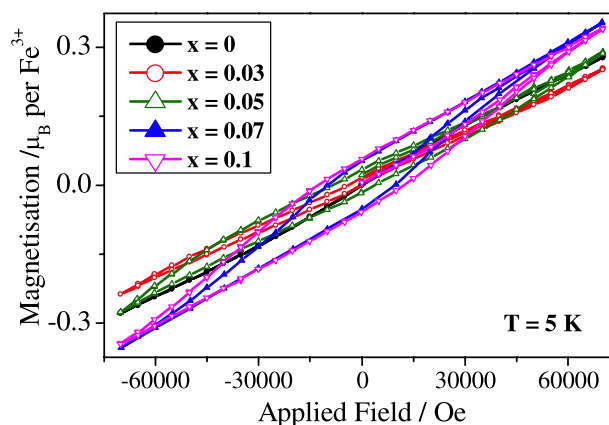

Figure 6. Magnetic hysteresis loops for polycrystalline $Bi_{1-x}Ca_xFeO_{3-x/2}$ samples measured at 5 K.

as a function of temperature reveal the existence of at least two structural phase transitions. The associated transition temperatures, defined as T_{C1} and T_{C2}, are given in table 2 and figure 9. Both T_{C1} and T_{C2} in $BiFeO_3$ decrease linearly with calcium doping but with noticeably different rates. A linear fitting reveals that the rates of change of T_{C1} and T_{C2} are ~ 50.5 K mol.% Ca^{2+} and ~ 1.8 K mol.% Ca^{2+}, respectively. An extrapolation of the fitted lines to $x = 0.0$ (pure $BiFeO_3$) gives $T_{C1} = 1072(18)$ K and $T_{C2} =$

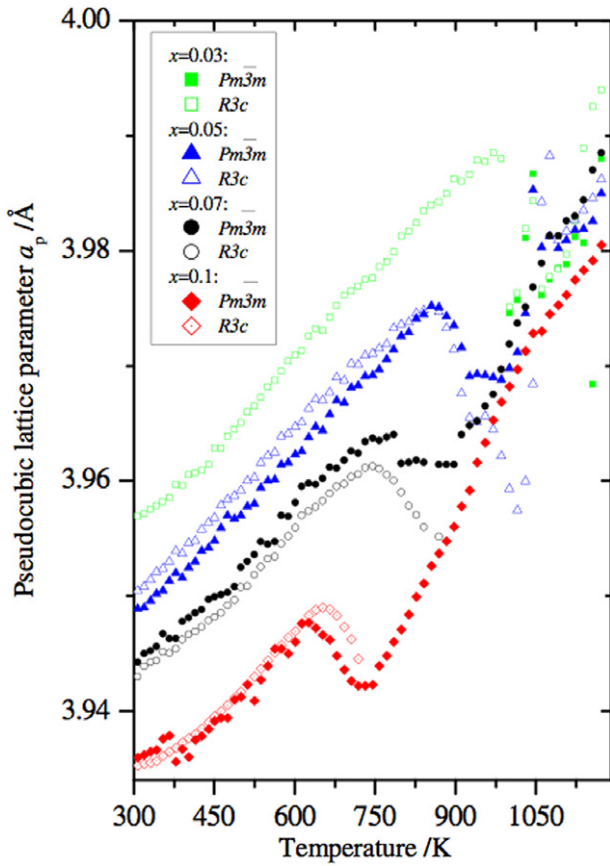**Figure 7.** Variation of the pseudo-cubic lattice parameter as a function of temperature for $x = 0.03$–0.1 in $Bi_{1-x}Ca_xFeO_{3-x/2}$ determined by Rietveld refinement of *in situ* powder XRD patterns. Both the cubic space group $Pm\bar{3}m$ and the rhombohedral space group $R3c$ were used as starting models depending on the temperature regions and samples of interest. The cubic model was used between 300 and 1175 K (for $x = 0.05, 0.07, 0.1$) and 1000–1175 K (for $x = 0.03$). The rhombohedral model was used between, 300 and 1175 K (for $x = 0.03$ and 0.05), 300–870 K (for $x = 0.07$) and 300–720 K (for $x = 0.1$). All data were recorded during heating in air. The higher transition temperature, T_{C2}, is revealed by the change in thermal expansion seen around 1050 K, while the lower transition is associated with a large change in lattice parameter (cell volume) which varies strongly with composition.

Table 2. Two structural phase transition temperatures, T_{C1} and T_{C2}, respectively, evaluated from *in situ* XRD analysis. (a) x: mole fraction of Ca^{2+} in $Bi_{1-x}Ca_xFeO_{3-x/2}$ and (b) T_C: ferroelectric Curie temperature determined by Yang *et al* [17].

$x^{(a)}$	T_{C1} (K)	$T_C^{(b)}$ (K)	T_{C2} (K)
0.03	985	982	1061
0.05	911	900	1061
0.07	799	756	1076
0.1	678	600	1045

1142(26) K. The structural phase transition temperature T_{C1} has been regarded as the ferroelectric Curie temperature T_C in BiFeO$_3$ for many years [17]. Present analysis shows that T_{C1} reduces drastically with Ca^{2+} doping. Our results are quite similar to those of Chaigneau *et al* [46] and Levin *et al* [47] who studied Pb^{2+} and Nd^{3+}-doped BiFeO$_3$. This indicates that doping with Pb^{2+} and/or Ca^{2+} in BiFeO$_3$ reduces the
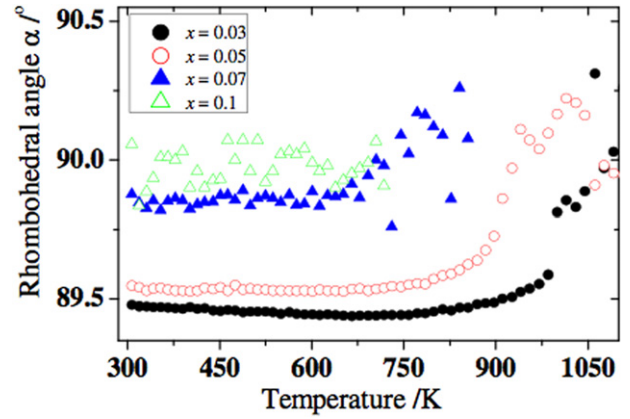

Figure 8. Variation of the rhombohedral angle (α) with temperature for different compositions. The angle was determined by employing the rhombohedral space group $R3c$ as a starting model to refine the lattice parameter.
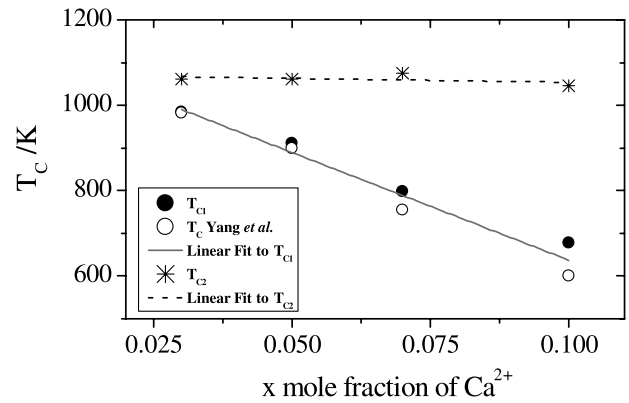

Figure 9. Variation of the structural phase transition temperatures (T_{C1} and T_{C2}) with mole fraction of Ca^{2+} in polycrystalline $Bi_{1-x}Ca_xFeO_{3-x/2}$ determined by *in situ* XRD analysis. For comparison, the ferroelectric T_C of Ca-doped BiFeO$_3$ thin films reported in Figure 1 of [17] has been incorporated. All T_{C1} values (from the present work and [17]) were used to fit a straight line.

ferroelectric ordering temperature. Furthermore, the effect of doping on the different rates of change of the two critical temperatures is consistent with the known behaviour of the α–β and β–γ phase transitions of pure BiFeO$_3$. The α–β (ferroelectric–paraelectric) transition changes the symmetry of the system and is associated with a very large volume contraction [48, 49], while the β–γ (metal–insulator) phase transition is isostructural and has a much smaller volume contraction [50]. Additionally, with increasing Ca^{2+} doping level, one should expect that the concentration of oxygen vacancies increases. Self-ordering of a large number of vacancies in the perovskite oxides can cause a structural phase transition (for example, this is well known in the perovskite to brownmillerite structural phase transition in CaFeO$_{2.5}$ [51]). Thus, the recent observation of the emergence of a brownmillerite-type phase in heavily Ca^{2+}-doped BiFeO$_3$ by Schiemer *et al* [21] is easily understood. In the present lightly doped system ($x \leq 0.1$) the vacancies created by doping can be considered to remain as uncorrelated clusters. There is a possibility that migration of these clusters also plays a role in reducing the structural phase
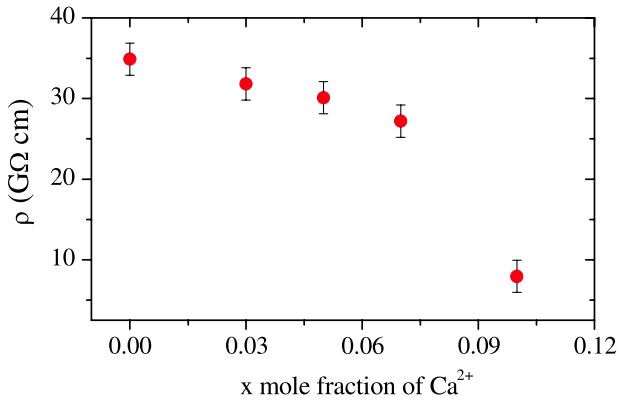
Figure 10. Variation of resistivity with fraction (x) of calcium on the A site measured at room temperature on sintered pellets.

transition temperature in this system. Combining the above discussion with our previous report (increase of T_N with Ca^{2+} doping [18]) it follows that a doping concentration of approximately 8.5 mol.% of Ca^{2+} in $BiFeO_3$ will result in the same critical temperature for both ferroelectric and antiferromagnetic ordering. Thus, one should expect the maximum magneto-electric coupling in $Bi_{1-x}Ca_xFeO_{3-x/2}$ at this composition. We attempted to measure the ferroelectric hysteresis loops, but all the doped samples exhibit poor P–E hysteresis loops due to large leakage currents. This is in agreement with Chen *et al* [20]. Thus, high frequency (GHz) magneto-dielectric measurements on this system may be used to test the above hypothesis.

The large room temperature conductivity of Ca^{2+}-doped $BiFeO_3$ has already been reported for thin films [17]. The resistivity (ρ) values measured for our Ca^{2+}-doped polycrystalline samples are 3.49×10^{10} ($x = 0.00$), 3.18×10^{10} ($x = 0.03$), 3.01×10^{10} ($x = 0.05$), 2.72×10^{10} ($x = 0.05$) and 0.795×10^{10} ($x = 0.1$) Ω cm, at room temperature. It is interesting to note that the resistivity reduces by almost an order of magnitude within 10 mol.% Ca^{2+} doping (figure 10). Given the underlying coupling between structure, extrinsic defect (oxygen vacancies) concentration and conductivity in these materials (including a metal–insulator transition at the high-temperature beta–gamma transition of pure $BiFeO_3$ [2, 48]) and in view of the large structural changes induced by doping in our samples, we measured the resistance as a function of temperature for all our samples in the high-temperature region. Figure 11 shows the resistivity behaviour as a function of temperature. No clear anomaly is observed in the temperature region where the structural and magnetic phase transitions take place. This is in partial agreement with Selbach *et al* [52]. For each composition, in the temperature range of 573–1173 K, plots of ln ρ as a function of $1/T$ exhibit two separate temperature regions where a linear dependence is observed. The linearity is characteristic of a system with a well-defined bandgap such that $\rho(T) \sim \exp(E_a/k_BT)$, where E_a is the thermal activation energy and k_B is the Boltzmann constant. The two straight lines yield two E_a values as shown in figure 11. The E_a values in the low- and high-temperature regions are estimated to be 0.4–0.7 and 0.03–0.16 eV, respectively. This suggests that the conduction in Ca^{2+}-doped
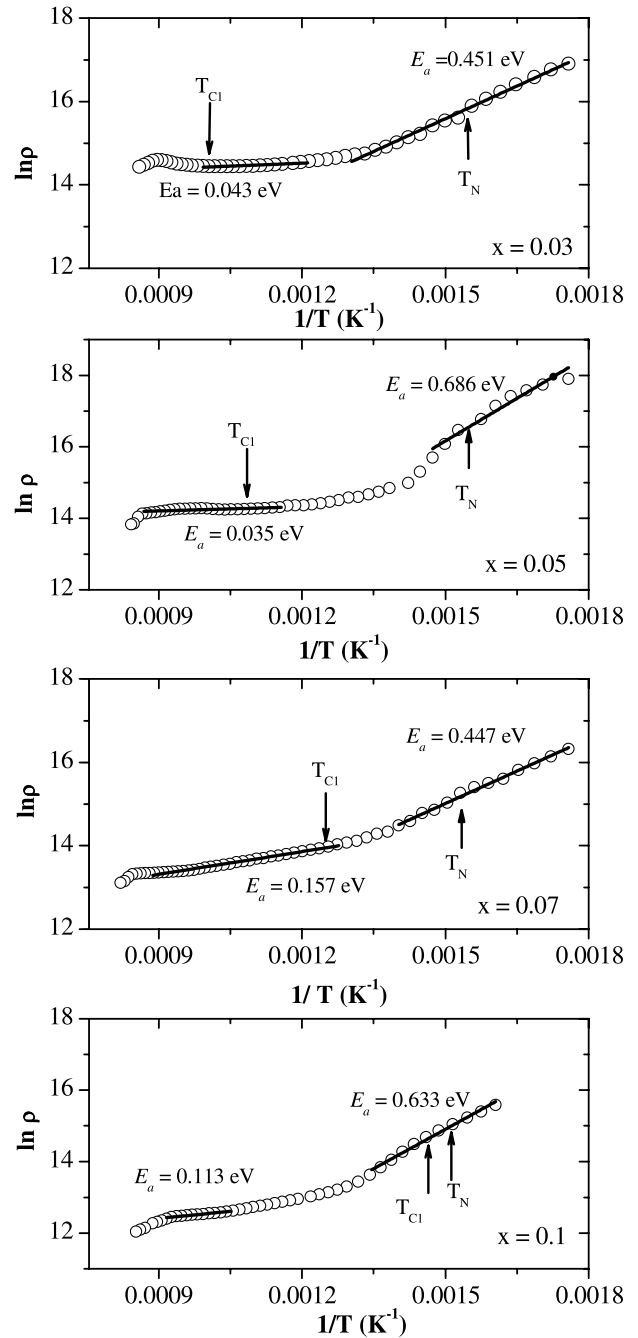

Figure 11. Arrhenius plots of resistivity of $Bi_{1-x}Ca_xFeO_{3-x/2}$ samples for $x = 0.03$–0.1. E_a is the activation energy as described in the text. The structural and antiferromagnetic phase transition temperatures are indicated with arrows.

$BiFeO_3$ is mainly governed by thermally activated hopping of electrons between oxygen-vacancy-related defects which is inconsistent with the vacancy-assisted electronic conduction mechanism observed recently in epitaxial thin films [17].

4. Conclusions

We have shown that samples of composition $Bi_{1-x}Ca_x FeO_{3-x/2}$ form a solid solution for $x \leq 0.1$, with the octahedral cation remaining Fe^{3+} throughout and charge compensation achieved through oxygen vacancy substitution.

The introduction of oxygen vacancies and of Ca on the A site appears to be stochastic, with no indication of long-range ordering (as would be indicated by brownmillerite-type structures). It therefore stabilizes the high-symmetry high-temperature polymorphs of $Bi_{1-x}Ca_xFeO_{3-x/2}$ with transition temperatures for the $\alpha-\beta$ phase transition dropping in temperature with increased Ca content. Magnetic measurements demonstrate that these samples are all antiferromagnetic, but that increased Ca incorporation leads to weak canted ferromagnetism. Finally, electrical conduction in these samples occurs via oxygen vacancy hopping, as revealed by the thermally activated behaviour shown in our data.

Acknowledgments

References

[1] Eerenstein W, Mathur N D and Scott J F 2006 *Nature* **442** 759
[2] Catalan G and Scott J F 2009 *Adv. Mater.* **21** 2463
[3] Sosnovska I, Peterlin-Neumaier T and Steichele E 1982 *J. Phys. C: Solid State Phys.* **15** 4835
[4] Roginska Y E, Tomashpo Y Y, Venevtse Y N, Petrov V M and Zhdanov G S 1966 *Sov. Phys.—JETP* **23** 47
[5] Zeches R J *et al* 2009 *Science* **326** 977
[6] Wang J *et al* 2003 *Science* **299** 1719
[7] Neaton J B, Ederer C, Waghmare U V, Spaldin N A and Rabe K M 2005 *Phys. Rev.* B **71** 014113
[8] Ravindran P, Vidya R, Kjekshus A, Fjellvåg H and Eriksson O 2006 *Phys. Rev.* B **74** 224412
[9] Valant M, Axelsson A and Alford N 2007 *Chem. Mater.* **19** 5431
[10] Lee D, Kim M G, Ryu S, Jang M H and Lee S G 2005 *Appl. Phys. Lett.* **86** 222903
[11] Yoneda Y, Yoshii K, Saitoh H and Mizuki J 2007 *Ferroelectrics* **348** 33
[12] Troyanchuk I O, Bushinsky M V, Karpinsky D V, Mantytskaya O S, Fedotova V V and Prochnenko O I 2009 *Phys. Status Solidi* **246** 1901
[13] Khomchenko V A, Kiselev D A, Vieira J M, Jian Li, Kholkin A L, Lopes A M L, Pogorelov Y G, Araujo J P and Maglione M 2008 *J. Appl. Phys.* **103** 024105
[14] Khomchenko V A, Paixãoa J A, Kiselev D A and Kholkin A L 2010 *Mater. Res. Bull.* **45** 416
[15] Cheng C-J, Kan D, Lim S-H, McKenzie W R, Munroe P R, Salamanca-Riba L G, Withers R L, Takeuchi I and Nagarajan V 2009 *Phys. Rev.* B **80** 014109
[16] Yuan G L, Or Siu Wing, Liu J M and Liu Z G 2006 *Appl. Phys. Lett.* **89** 052905
[17] Yang C-H *et al* 2009 *Nat. Mater.* **8** 485
[18] Catalan G, Sardar K, Church N S, Scott J F, Harrison R J and Redfern S A T 2009 *Phys. Rev.* B **79** 212415
[19] Chen S, Wang L, Xuan H, Zheng Y, Wang D, Wu J, Du Y and Huang Zhigao 2010 *J. Alloy Compd.* **506** 537
[20] Chen W, Williams A J, Ortega-San-Martin L, Li M, Sinclair D C, Zhou W and Paul Attfield J 2009 *Chem. Mater.* **21** 2085
[21] Schiemer J, Withers R, Norn L, Liu Y, Bourgeois L and Stewart G 2009 *Chem. Mater.* **21** 4223
[22] Kothari D, Reddy V R, Gupta A, Sathe V, Banerjee A, Gupta S M and Awasthi A M 2007 *Appl. Phys. Lett.* **91** 202505
[23] Khomchenko V A *et al* 2009 *J. Magn. Magn. Mater.* **321** 1692
[24] Khomchenko V A, Kiselev D A, Selezneva E K, Vieira J M, Lopes A M L, Pogorelov Y G, Araujo J P and Kholkin A L 2008 *Mater. Lett.* **62** 1927
[25] Ghosh S, Dasgupta S, Sen A and Maiti H S 2005 *J. Am. Ceram. Soc.* **88** 1349
[26] Larson A C and Dreele R B V 1994 *Los Alamos National Laboratory Report LAUR* pp 86–748
[27] Toby B H 2001 *J. Appl. Cryst.* **34** 210
[28] Dent A J, Cibin G, Ramos S, Smith A D, Scott S M, Varandas L, Pearson M R, Krumpa N A, Jones C P and Robbins P E 2009 *J. Phys. Conf. Ser.* **190** 012039
[29] Ravel B and Newville M 2005 *J. Synchrotron. Radiat.* **2** 537
[30] Lebeugle D, Colson D, Forget A, Viret M, Bataille A M and Gukasov A 2008 *Phys. Rev. Lett.* **100** 227602
[31] Schmid H 2008 *J. Phys.: Condens. Mater.* **20** 434201
[32] Moreau J M, Michel C, Gerson R and James W J 1971 *J. Phys. Chem. Solids* **32** 1315
[33] Li J, Duan Y, He H and Song D 2001 *J. Alloys Compounds* **315** 259
[34] Lepoittevin C, Malo S, Barrier N, Nguyen N, Van Tendeloo G and Hervieu M 2008 *J. Solid State Chem.* **181** 2601
[35] Haumont R, Kreisel J and Bouvier P 2009 *Phase Transit.* **82** 496
[36] Karimi S, Reaney I M, Han Y, Pokorny J and Sterianou I 2009 *J. Mater. Sci.* **44** 5102
[37] Berry A J, O'Neill H S, Jayasuriya K D, Campbell S J and Foran G J 2003 *Am. Mineral.* **88** 967
[38] Binsted N, Greaves G N and Henderson C M B 1985 *Contrib. Min. Pet.* **89** 103
[39] Qin Y B, Yang H X, Zhang Y, Tian H F, Ma C, Zhao Y G, Walton R I and Li J Q 2009 *J. Phys.: Condens. Matter* **21** 015401
[40] Jun Y, Lee S, Kim M, Hong S B, Kim J W and Kim K H 2007 *J. Mater. Res.* **22** 3397
[41] Lee D, Kim M G, Ryu S and Jang H M 2005 *Appl. Phys. Lett.* **86** 222903
[42] Lebeugle D, Colson D, Forget A, Viret M, Bonville P, Marucco J F and Fusil S 2007 *Phys. Rev.* B **76** 024 116
[43] Zhou H D and Goodenough J B 2005 *Solid State Sci.* **7** 656
[44] Maljuk A, Strempfer J and Lin C T 2003 *J. Cryst. Growth* **258** 435
[45] Kadomtseva A M, Popov Yu F, Pyatakova A P, Vorob'ev G P, Zvezdin A K and Viehland D 2006 *Phase Transit.* **79** 1019
[46] Chaigneau J, Haumont R and Kiat J M 2009 *Phys. Rev.* B **80** 184107
[47] Levin I, Karimi S, Provenzano V, Dennis C L, Wu H, Comyn T P, Stevenson T J, Smith R I and Reaney I M 2010 *Phys. Rev.* B **81** 020103
[48] Palai R, Katiyar R S, Schmid H, Tissot P, Clark S J, Robertson J, Redfern S A T, Catalan G and Scott J F 2008 *Phys. Rev.* B **77** 014110
[49] Arnold D C, Knight K S, Morrison F D and Lightfoot P 2009 *Phys. Rev. Lett.* **102** 027602
[50] Arnold D C, Knight K S, Catalan G, Redfern S A T, Scott J F, Lightfoot P and Morrison F D 2010 *Adv. Funct. Mater.* **20** 2116
[51] Becerro A I, Redfern S A T, Carpenter M A, Knight K S and Seifert F 2002 *J. Solid State Chem.* **167** 459
[52] Selbach S, Tybell T, Einarsrud M and Grande T 2008 *Adv. Mater.* **20** 3682